# Collective aspects deduced from time-dependent microscopic mean-field with pairing: Application to the fission process

Yusuke Tanimura,[1,*] Denis Lacroix,[1,†] and Guillaume Scamps[2,‡]
[1]*Institut de Physique Nucléaire, IN2P3-CNRS, Université Paris-Sud, F-91406 Orsay Cedex, France*
[2]*Department of Physics, Tohoku University, Sendai 980-8578, Japan*
(Received 21 May 2015; published 1 September 2015)

Given a set of collective variables, a method is proposed to obtain the associated conjugated collective momenta and masses starting from a microscopic time-dependent mean-field theory. The construction of pairs of conjugated variables is the first step to bridge microscopic and macroscopic approaches. The method is versatile and can be applied to study a large class of nuclear processes. An illustration is given here with the fission of $^{258}$Fm. Using the quadrupole moment and eventually higher-order multipole moments, the associated collective masses are estimated along the microscopic mean-field evolution. When more than one collective variable is considered, it is shown that the off-diagonal matrix elements of the inertia play a crucial role. Using the information on the quadrupole moment and associated momentum, the collective evolution is studied. It is shown that dynamical effects beyond the adiabatic limit are important. Nuclei formed after fission tend to stick together for a longer time leading to a dynamical scission point at a larger distance between nuclei compared to the one anticipated from the adiabatic energy landscape. The effective nucleus-nucleus potential felt by the emitted nuclei is finally extracted.

DOI: 10.1103/PhysRevC.92.034601 PACS number(s): 24.75.+i, 21.60.Jz, 27.90.+b

## I. INTRODUCTION

Nuclear time-dependent mean-field based on the energy density functional approach is experiencing nowadays a renewal of interest [1–6]. In particular, it allows one to describe a wide variety of dynamical processes ranging from small to large amplitude collective motions, including nuclear reactions. Among the most difficult challenges one can mention is the description of nuclear fission where a single nucleus encounters large deformation leading finally to separated fragments.

Although the fission process is quite well understood phenomenologically [7], it still remains one of the most difficult processes to describe microscopically. One of the major difficulties is the necessity to treat collective and single-particle degrees of freedom (DOF) simultaneously as quantum objects [8]. Moreover, fission is a dynamical process and therefore should be treated as such. To describe the dynamic of fission, one can *a priori* use two strategies. Using the fact that the time scale associated to fission is rather large, the most common starting point is to first select a few collective DOFs and generate an adiabatic energy landscape. Then, the time scale associated to fission can be evaluated using semiclassical approximation. Alternatively, the real time dynamic can be explicitly followed using for instance the time-dependent generator coordinates method [9]. Two important problems are generally encountered in this strategy. First, this approach can hardly accommodate too many collective DOFs due to the increasing complexity. Second, while rather slow, the dynamics of fission might deviate from the completely adiabatic path when the two fragments approach the scission.

An alternative strategy is to use microscopic quantum transport theories such as the time-dependent energy density functional (TD-EDF) theory. This approach offers the possibility to describe some aspects of the fission process without assuming adiabaticity while leaving the possibility to explore rather complex shapes during the separation process. In addition, the recent inclusion of dynamical pairing has opened new perspectives [10–15]. On the other hand, the TD-EDF approach cannot describe completely the fission process due to the absence of spontaneous symmetry breaking and due to poor treatment of quantal effects in collective space. However, it can still provide important information in particular after the system has passed the fission barrier. This has been illustrated in Refs. [16–18] and more recently in Ref. [19].

The TD-EDF directly performs the evolution of single-particle states in a self-consistent mean-field. From this evolution, one can directly infer the information on any one-body degree of freedom like multipole deformation, neck formation, and/or fragment separation, final kinetic energies, etc. The aim of the present work is to explore the possibility to get macroscopic transport coefficients, like collective mass, collective potential, or energy dissipation, directly from TD-EDF. In particular, this should allow us to compare the results of TD-EDF to similar quantities generally obtained in the adiabatic limit and/or macroscopic models.

In the following, we analyze first how collective masses and momenta can be associated to given collective observables along a microscopic mean-field path. Once the pairs of conjugated operators are available, a macroscopic reduction of the microscopic approach can be made to give physical insights. For the fission process, the energy sharing between internal and selected DOFs can be precisely scrutinized.

*tanimura@ipno.in2p3.fr
†lacroix@ipno.in2p3.fr
‡scamps@nucl.phys.tohoku.ac.jp

 

## II. COLLECTIVE MASS AND MOMENTUM EXTRACTED FROM DYNAMICAL MEAN-FIELD THEORY

In the present section, we assume that the mean-field trajectory, including or not including pairing, is known, leading to a specific trajectory in the Liouville space of the normal and anomalous density matrices $(\rho(t),\kappa(t))$. Starting from these densities, we want to extract information on a set of given collective variables. Note that, although we present examples specifically on the fission process, the approach developed here is general and can be applied to other processes.

### A. TD-EDF evolution of one-body operators

Before starting the main subject of the present work, we recall some aspects of TD-EDF with pairing. The matrix elements of the normal and anomalous densities are defined through

$$\rho_{ij}(t) = \langle \hat{a}_j^\dagger \hat{a}_i \rangle, \quad \kappa_{ij}(t) = \langle \hat{a}_j \hat{a}_i \rangle,$$

where $(\hat{a}_i^\dagger,\hat{a}_i)$ correspond to creation/annihilation operators of a complete set of single-particle states. The expectation values are taken on the trial quasiparticle vacuum that is evolved in time. The TD-EDF equations of motion are similar to the time-dependent Hartree-Fock-Bogoliubov (TD-HFB) ones and can be written as (see for instance [20])

$$i\hbar\frac{d}{dt}\rho = [h(\rho),\rho] + \kappa\Delta^* - \Delta\kappa^*, \tag{1}$$

$$i\hbar\frac{d}{dt}\kappa = h(\rho)\kappa + \kappa h^*(\rho) - \rho\Delta - \Delta\rho^* + \Delta. \tag{2}$$

Here $h(\rho)$ and $\Delta$ are respectively the mean-field and pairing field matrix. These operators can be generically written as

$$h(\rho)_{ij} = \left(\frac{p^2}{2m}\right)_{ij} + U_{ij}(\rho) = \left(\frac{p^2}{2m}\right)_{ij} + \sum_{kl} v^M_{ikjl}\rho_{lk}, \tag{3}$$

$$\Delta_{ij} = \frac{1}{2}\sum_{kl} v^P_{ijkl}\kappa_{kl}, \tag{4}$$

where $U$ is the mean-field potential. Here $v^M$ and $v^P$ denote the effective vertex respectively in the particle-hole and particle-particle channels and can be directly defined as functional derivatives of the energy. In the nuclear context, the difference between TD-HFB and TD-EDF stems from the flexibility in choosing the effective interactions.

Let us consider a general one-body operator $\hat{Q}$ with

$$\hat{Q} = \sum_{ij}\langle i|\hat{Q}|j\rangle \hat{a}_i^\dagger \hat{a}_j. \tag{5}$$

Its expectation value along the TD-EDF path is given by $\langle\hat{Q}\rangle = \mathrm{Tr}(Q\rho)$. Therefore, its evolution writes

$$i\hbar\frac{d\langle\hat{Q}\rangle}{dt} = i\hbar\mathrm{Tr}\left(Q\frac{d\rho}{dt}\right) = \mathrm{Tr}(Q[h(\rho),\rho]) + \mathrm{Tr}(Q[\kappa\Delta^* - \Delta\kappa^*]). \tag{6}$$

We restrict here the discussion to the case of zero range effective interaction in the pairing channel. More precisely, we assume that the interaction writes $g(\boldsymbol{r})\delta(\boldsymbol{r}-\boldsymbol{r}')(1-P_\sigma)/2$, where $g(\boldsymbol{r})$ is the strength ($\boldsymbol{r}$ dependence accounting for a density dependence) and $P_\sigma$ is the spin-exchange operator. This type of interaction is used in the present work as well as in most TD-EDF calculations with pairing correlation. Then the pairing field $\Delta$ is local in space and one has

$$\mathrm{Tr}(Q\kappa\Delta^*) = \mathrm{Tr}(Q\Delta\kappa^*) = 2\int d^3r\; g(\boldsymbol{r})Q(\boldsymbol{r})\kappa_{\uparrow\downarrow}(\boldsymbol{r})\kappa^*_{\downarrow\uparrow}(\boldsymbol{r}), \tag{7}$$

where $\kappa_{\sigma\sigma'}(\boldsymbol{r}) \equiv \kappa_{\mathbf{r}\sigma,\mathbf{r}\sigma'}$. Therefore the second term on the right hand side of Eq. (6) cancels out and

$$i\hbar\frac{d\langle\hat{Q}\rangle}{dt} = \mathrm{Tr}(Q[h(\rho),\rho]) = \mathrm{Tr}([Q,h(\rho)]\rho), \tag{8}$$

where the permutation property of the trace is used to obtain the last expression.

Note that even if the pairing field does not explicitly appear in the equation of motion of a normal operator, it contributes to the dynamics through its self-consistent influence on the one-body density given by Eq. (1).

In the present work, we further restrict the discussion to collective DOFs associated to the one-body operator $\hat{Q}_\alpha$ that are local in space. Using the eigenstates $|\boldsymbol{r}\rangle$ as a complete basis, Eq. (5) becomes

$$\hat{Q}_\alpha = \int d^3r\, Q_\alpha(\boldsymbol{r})\hat{\Psi}^\dagger(\boldsymbol{r})\hat{\Psi}(\boldsymbol{r}), \tag{9}$$

where $\hat{\Psi}^\dagger(\boldsymbol{r})$ and $\hat{\Psi}(\boldsymbol{r})$ are the creation/annihilation operators of a particle at position $\boldsymbol{r}$, and $Q_\alpha(\boldsymbol{r}) = \langle\boldsymbol{r}|\hat{Q}_\alpha|\boldsymbol{r}\rangle$ is the local matrix element of the operator $\hat{Q}_\alpha$. For the sake of simplicity, we omitted the spin and isospin quantum numbers. Note that most macroscopic DOFs of interest like multipole operators, relative distance, mass asymmetry, etc., correspond to expectation values of local one-body operators.

Along the mean-field trajectory, the collective evolution is given by

$$q_\alpha(t) \equiv \mathrm{Tr}[Q_\alpha\rho(t)] = \int Q_\alpha(\boldsymbol{r})n(\boldsymbol{r},t)d^3r, \tag{10}$$

where we have introduced the local density $n(\boldsymbol{r},t) = \rho_{\mathbf{rr}}(t)$. The first step to bridge the microscopic mean-field theory and a macroscopic-like evolution for the collective variable $q_\alpha$ is to find the corresponding conjugated momentum $p_\alpha$ and associated collective mass, denoted by $M_\alpha$. Assuming a classical equation of motion for $q_\alpha$, Eq. (8) should ultimately identify with an equation of motion of the form $\dot{q}_\alpha = p_\alpha/M_\alpha$.

In most TD-EDF approaches used nowadays, the functional is based on a zero-range Skyrme-like interaction. Then, the mean-field potential is also local in space, i.e., $\langle\mathbf{r}|\hat{U}|\mathbf{r}'\rangle = \delta(\mathbf{r}-\mathbf{r}')U(\mathbf{r})$, leading directly to

$$[\hat{Q}_\alpha,\hat{U}] = 0. \tag{11}$$

Reporting in Eq. (8), we finally obtain that

$$\frac{dq_\alpha}{dt} = -\frac{i}{2\hbar m}\mathrm{Tr}([Q_\alpha, p^2]\rho(t)) \equiv \frac{p_\alpha}{M_\alpha}, \tag{12}$$

where $m$ is the nucleon mass, and $p$ is the single-particle momentum matrix. From this expression, a simple guess for the conjugated momentum fulfilling the constraint $p_\alpha = \langle \hat{P}_\alpha \rangle$, is to assume that it can directly be defined through

$$\hat{P}_\alpha \equiv -i\frac{M_\alpha}{2\hbar m}\sum_{ij}\langle i|[\hat{Q}_\alpha, \hat{p}^2]|j\rangle \hat{a}_i^\dagger \hat{a}_j. \tag{13}$$

From this definition, using $p = -i\hbar\nabla$ and performing the commutator, one sees that the matrix elements of the operator $\hat{P}_\alpha$ in the position space are given by

$$P_\alpha \equiv -i\hbar\frac{M_\alpha}{m}\left(\frac{\nabla^2 Q_\alpha}{2} + \nabla Q_\alpha \cdot \nabla\right), \tag{14}$$

that is similar to the expression obtained in [21] using a variational principle around a static mean-field to study anharmonic effects in giant resonances.

One shortcoming of the above expression is that the operator $\hat{P}_\alpha$ contains the collective mass $M_\alpha$ that is unknown. To further progress, we seek for the condition that $(\hat{Q}_\alpha, \hat{P}_\alpha)$ are conjugated observables. Strictly speaking conjugated variables should fulfill the condition

$$[\hat{Q}_\alpha, \hat{P}_\alpha] = i\hbar. \tag{15}$$

Imposing this strict condition at all time seems rather complicated. A simpler condition that is used for instance in the time-dependent RPA (TD-RPA) [22] is to impose that this condition is fulfilled when the expectation value is performed on the TD-RPA ground state. In the TD-EDF case, this would transpose as imposing the condition

$$\langle [\hat{Q}_\alpha, \hat{P}_\alpha] \rangle = i\hbar, \tag{16}$$

where the expectation value is taken on the time-dependent quasiparticle vacuum. Using the commutation relation of one-body operators, we first note that

$$[\hat{Q}_\alpha, \hat{P}_\alpha] = \sum_{ij}\langle i|[Q_\alpha, P_\alpha]|j\rangle \hat{a}_i^\dagger \hat{a}_j. \tag{17}$$

Therefore, the constraint (16) can be equivalently written as the matrix element constraint,

$$\mathrm{Tr}(\rho(t)[Q_\alpha, P_\alpha]) = i\hbar, \tag{18}$$

along the trajectory. Using expression (13), we also have

$$\begin{aligned}\mathrm{Tr}\{[Q_\alpha, P_\alpha]\rho(t)\} &= -i\frac{M_\alpha}{2\hbar m}\mathrm{Tr}\{[Q_\alpha,[Q_\alpha, p^2]]\rho(t)\} \\ &= +i\hbar\frac{M_\alpha}{m}\mathrm{Tr}[\rho(t)\nabla Q_\alpha \cdot \nabla Q_\alpha].\end{aligned}$$

Therefore, we see that the condition (18) determines uniquely the collective mass through

$$\frac{1}{M_\alpha(t)} = \frac{1}{m}\mathrm{Tr}[\rho(t)\nabla Q_\alpha \cdot \nabla Q_\alpha], \tag{19}$$

all along the trajectory and henceforth also leads to an unambiguous definition of the collective momentum operator $\hat{P}_\alpha$ when reporting the mass in Eq. (14). A similar formula is sometimes used to compute collective mass from a microscopic adiabatic energy landscape (see for instance [23–25]). The difference is that this expression has been derived here without assuming adiabaticity. In addition, since the expectation value is directly performed using the time-dependent mean-field density it automatically contains possible influence of other DOFs as well as the pairing effects. Notice that the normal density $\rho(t)$ implicitly takes into account the pairing effect through the occupation numbers, which evolve under influence of interaction in the pairing channel. We also note here again that the derivation presented above relies on the assumptions that the effective interactions both in particle-hole and particle-particle channels are local and zero-range. The mass formula (19) is rather straightforward to calculate. We give illustration of some expressions obtained for specific collective operators in Appendix A.

Once the mass and the momentum are known, one can also define the collective kinetic energy corresponding to the selected variable as

$$E^\alpha_{\mathrm{kin}}(t) = \frac{p_\alpha^2(t)}{2M_\alpha} = \frac{1}{2}M_\alpha \dot{q}_\alpha^2(t). \tag{20}$$

### B. Generalization to several collective degrees of freedom

Let us now consider a more general case where a set of $N$ collective DOFs $\{Q_\alpha\}_{\alpha=1,N}$ are selected. A naive generalization to the previous section is to assign to each variable $Q_\alpha$, a collective momentum $P_\alpha$ with matrix elements given by Eq. (14). One should *a priori* also generalize the commutation relation (18). Using Eq. (14), we have

$$\langle [\hat{Q}_\alpha, \hat{P}_\beta] \rangle = i\hbar\frac{M_{\beta\beta}}{m}\mathrm{Tr}[\rho(t)\nabla Q_\alpha \cdot \nabla Q_\beta] = i\hbar\frac{M_{\beta\beta}}{M_{\alpha\beta}}, \tag{21}$$

where the off-diagonal mass matrix elements reads

$$\frac{1}{M_{\alpha\beta}(t)} = \frac{1}{m}\mathrm{Tr}[\rho(t)\nabla Q_\alpha \cdot \nabla Q_\beta]. \tag{22}$$

This expression naturally extends the previous case and was also given in Ref. [25]. As shown in Appendix B, the diagonalization of the mass gives new canonical pairs of collective operators $(\hat{Q}'_k, \hat{P}'_k)$, whose commutation rules identify with the TDRPA ones and are given by

$$\langle [\hat{Q}'_k, \hat{P}'_l] \rangle = i\hbar\delta_{kl}. \tag{23}$$

The diagonalization is equivalent also to removing the correlation among the variables like multipole moments.

These new operators are particularly useful to get simple expressions for the evolution and collective energy. In particular, we have $\dot{q}'_k = p'_k/M'_\alpha$ while the collective kinetic energy is simply given by

$$E^{\{\alpha\}}_{\mathrm{kin}} = \sum_k \frac{p'^2_k(t)}{2M'_k(t)}. \tag{24}$$

Once the set of collective variables is properly defined, macroscopic analysis of TD-EDF evolution can be made. Such a connection from the microscopic level to the macroscopic one is illustrated below for the fission process.

### III. APPLICATION TO THE FISSION OF $^{258}$Fm

To illustrate the method presented in the previous section, we consider the case of $^{258}$Fm that was the subject of the recent work [19]. This nucleus is anticipated to have three different paths towards fission. In this work, we concentrate on the so-called symmetric compact shape. The energy landscape is obtained using the EV8 program with a constraint of the quadrupole moment [26]. We use here the standard definition for multipole moments

$$Q_\lambda = \sqrt{\frac{16\pi}{2\lambda+1}}\langle \hat{r}^\lambda \hat{Y}_{\lambda 0}\rangle, \tag{25}$$

leading for instance to $Q_2 = \langle 2\hat{z}^2 - \hat{x}^2 - \hat{y}^2\rangle$.

An illustration of the potential energy curve (PEC) is shown in Fig. 1 as a function of the quadrupole moment $Q_2$. As in Ref. [19], the Sly4d Skyrme functional [1] is used for the mean-field channel while a constant interaction is retained for the pairing channel. The static calculations are performed with a mesh size $13.2 \times 24.4 \times 13.2$ fm$^3$ and a mesh step $\Delta x = 0.8$ fm.

The dynamical evolution of the system starting from any point of the PEC can be made consistently using the recently developed TD-EDF code including pairing in the BCS approximation [15,27,28]. Dynamical calculations shown here are performed in a mesh of size $26.4 \times 72.8 \times 13.2$ fm$^3$ with the same mesh step as in the static case $\Delta x = 0.8$ fm. The time step is $\Delta t = 1.5 \times 10^{-24}$ sec $\approx$0.45 fm/c. In the present calculations, reflection and axial symmetries are assumed in the constrained calculation. Since symmetry cannot be broken spontaneously by mean-field, only even multipole moments

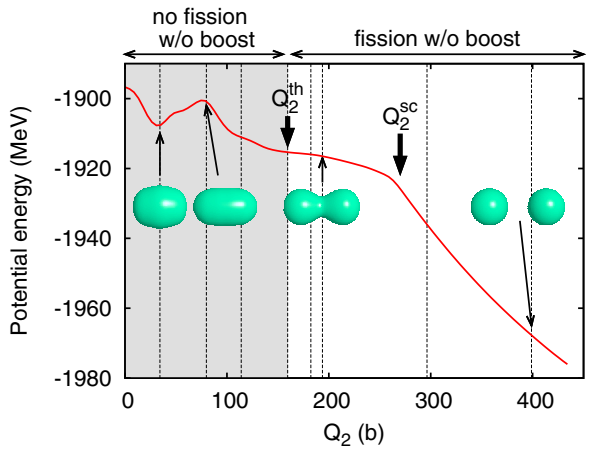


FIG. 1. (Color online) Potential energy curve of $^{258}$Fm nucleus as a function of the quadrupole deformation parameter (in barn units). Isosurfaces of the total density drawn at half the maximum value at $Q_2 = 34$, 80, 194, and 399 b are also shown. The horizontal lines indicate the different starting points that are used in this work as initial conditions for the time-dependent evolution. The different vertical dashed lines corresponds from left to right to $Q_2 = 34.2$ b, $Q_2 = 80$ b (barrier position), $Q_2 = 160$ b (spontaneous fission threshold $Q_2^{\rm th}$), $Q_2 = 182$ b, $Q_2 = 194$ b, $Q_2 = 296$ b, and $Q_2 = 400$ b. The two thick arrows indicate the spontaneous fission threshold $Q_2^{\rm th}$ and the adiabatic scission point $Q_2^{\rm sc}$.

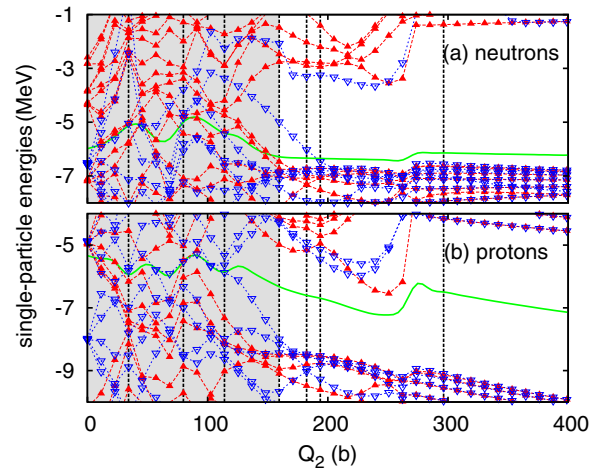


FIG. 2. (Color online) Single-particle energies in $^{258}$Fm nucleus along the adiabatic PEC. The green solid curves show the neutron and proton Fermi energies. Positive and negative parity states are respectively shown with red filled and blue open triangles. The vertical lines indicate the initial values of the quadrupole moment taken in the present dynamical calculations. The shaded area presenting the region where the system does not spontaneously fission is also shown.

can be nonzero during the evolution. In particular, we do not consider here possible octupole deformation.

As it was observed previously including or not including pairing, the system will spontaneously separate into two fragments only above a certain value of the initial quadrupole moment, which is larger than that of the fission barrier shown in Fig. 1 [16–19]. The lowest initial quadrupole moment leading to spontaneous fission within TD-EDF is called hereafter "dynamical fission threshold" and will be denoted by $Q_2^{\rm th}$. In the present calculation, the threshold deformation is approximately $Q_2^{\rm th} \simeq 160$ b. The shaded area in this figure indicates the region where the system does not spontaneously fission. The fact that $Q_2^{\rm th}$ is well beyond the expected barrier position points out the deviation from the adiabatic limit of the microscopic transport theory close to the single-particle levels crossing. This point was already discussed in Ref. [16]. To illustrate the connection between the dynamical fission threshold and level crossing, the single-particle energies evolution obtained in the static constrained mean-field are shown in Fig. 2 as a function of $Q_2$.

We see in particular that for large $Q_2$ a gap in single-particle energies appears that shows the transition from one to two nuclei. At low quadrupole moments, many crossings occur. When one leaves the system initially in the shaded area, single-particle wave functions will evolve in time. However, the motion is not adiabatic and both occupations above and below the Fermi energy will be populated in time. The PEC is meaningful only if lowest levels are preferentially occupied during the evolution while higher levels are depopulated. TD-EDF including or not including pairing does not lead to sufficient reorganization of single-particle occupation numbers during the crossing to follow the adiabatic PEC as has already been realized in Refs. [16–19]. As studied in Ref. [17], the system initialized inside the shaded area can still fission if, for

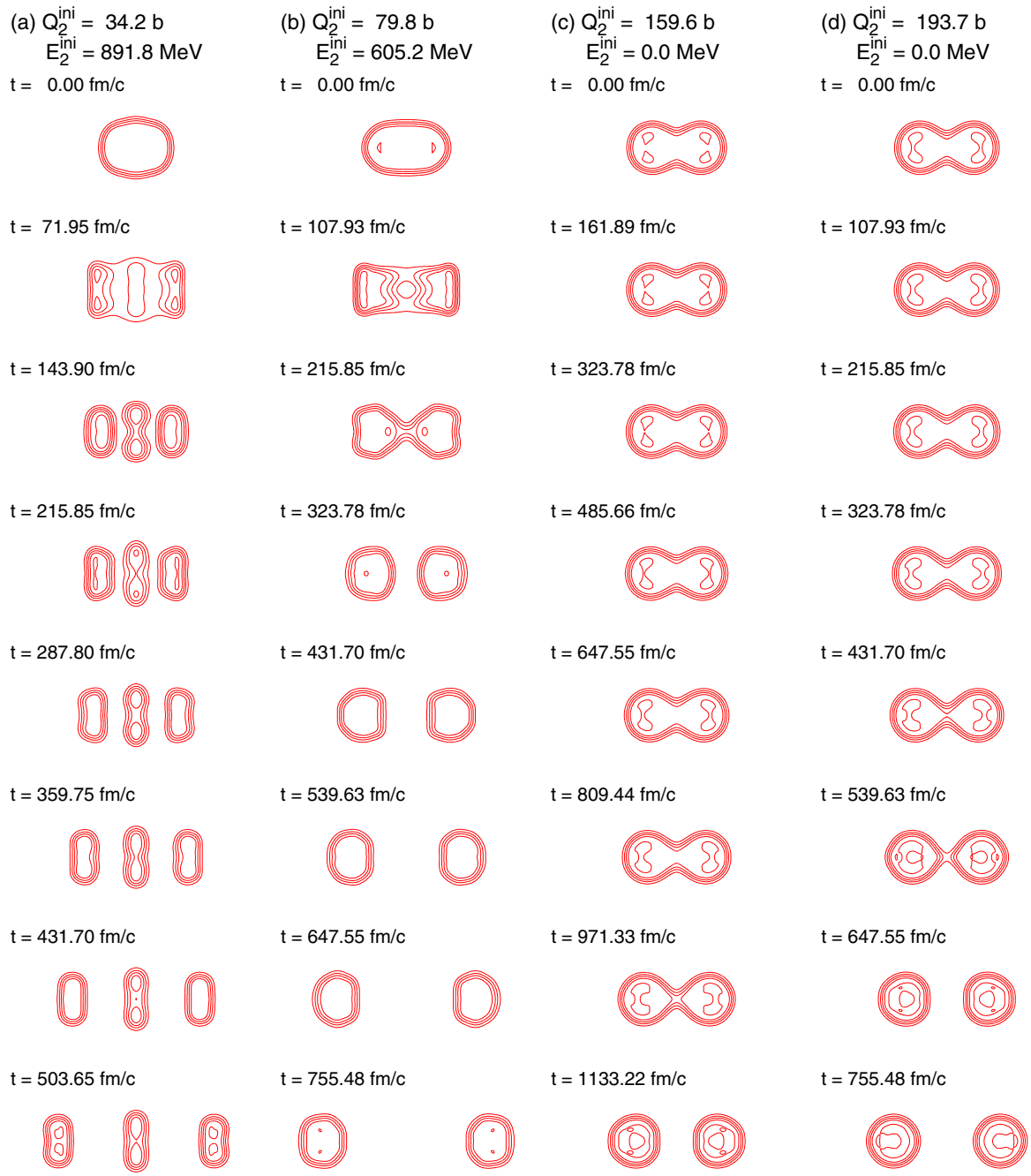


FIG. 3. (Color online) Density profiles obtained for different initial $Q_2$. The densities are shown as a function of time. For initial $Q_2$ below the fission threshold, a quadrupole boost has been imposed initially. From left to right, the initial $Q_2$ values are $Q_2 = 34.2$ b, $Q_2 = 80$ b, $Q_2 = 160$ b, and $Q_2 = 194$ b. The system is eventually initially boosted leading to nonzero values of $E_2^{\rm ini}$ directly indicated in the figure. The isodensity curves are drawn from 0.03 to 0.15 fm$^{-3}$ with increments of 0.03 fm$^{-3}$.

instance, a boost in the quadrupole momentum is applied at initial time. In practice, the boost is imposed by applying the local operator $\exp[ip_2 Q_2(\boldsymbol{r})/\hbar]$ to each single-particle wave function. This induces an additional initial collective kinetic energy [17]

$$E_2^{\rm ini} = \frac{p_2^2}{2m} \int |\nabla Q_2(\boldsymbol{r})|^2 n(\boldsymbol{r}, t=0) d^3r,$$

where $n(\boldsymbol{r},t=0)$ denotes the local density of the system in the adiabatic curve selected at a given initial moment. Note that $E_2^{\rm ini} = p_2^2/(2M_2)$ with the quadrupole mass given by Eq. (19).

In Fig. 3, several examples of density evolution obtained for different initial conditions including or not including a boost initially and leading to fission are illustrated. We see that a variety of phenomena including ternary fission in some cases can be observed.

### A. Mass parameter from TD-EDF

In the present section, we consider different initial quadrupole deformations between the fission barrier and the scission point. The scission point corresponding to a quadrupole deformation $Q_2^{\rm sc}$ can already be seen as shown in Fig. 1. It corresponds to the kink in the PEC appearing at $Q_2 \simeq 270$ b. After the scission point, the PEC is nearly dominated by the Coulomb interaction between the two fragments (see also Fig. 8).

As an illustration, we consider that the initial state corresponds to $Q_2^{\rm ini} = 160$ b, that is a situation just above the spontaneous fission threshold. This initial condition is similar to the one considered in Ref. [19]. In particular, it has been shown that if the system is left initially with zero collective energy, the total final kinetic energy of fragments after TD-EDF evolution is compatible with experimental observation. To study the possible nonadiabatic effect, initial conditions with boost of varying intensity (including no boost at all) are used.

The quadrupole moment is selected as the most relevant collective DOF. Using Eq. (19), the associated collective mass is then given by (see Appendix A)

$$\frac{1}{M_\alpha} = \frac{4}{m}(2\langle \hat{r}^2\rangle + \langle \hat{Q}_2\rangle), \tag{26}$$

where $\langle \hat{r}^2\rangle$ and $\langle \hat{Q}_2\rangle$ are respectively the root-mean-square radius and quadrupole moment along the path.

To get physical insight it is interesting to consider the situation where the system is already about to get separated into two fragments with a neck. Assuming simply that the neck position is at the center of the whole system, quantities like mass, position, momentum, and intrinsic deformations of each fragment can be estimated through

$$\langle \hat{X}\rangle_{[1]} = \int X(\boldsymbol{r}) n(\boldsymbol{r},t)\Theta(z) d^3r,$$

$$\langle \hat{X}\rangle_{[2]} = \int X(\boldsymbol{r}) n(\boldsymbol{r},t)[1-\Theta(z)] d^3r,$$

where $\hat{X}$ and $X(\boldsymbol{r})$ are the local operator and its local matrix element, respectively, corresponding to the specific quantity under interest, $\Theta(z)$ is the Heaviside step function, and $[i = 1,2]$ is a label of fragments. For a dinuclear system, the quadrupole mass can be recast as

$$\frac{1}{M_2} = \frac{8\mu(t)}{m^2}R^2(t) + \frac{4}{m}\sum_{i=1,2}[2\langle \hat{r}^2\rangle_{[i]} + \langle \hat{Q}_2\rangle_{[i]}],$$

where $\mu(t) = mA_1A_2/A$ is the reduced mass of the system and $R(t)$ is the relative distance between the center of mass of the two fragments.

At very large distance, $R(t) \to +\infty$, we see that the mass is dominated by the first term and tends to infinity. For display purposes we consider, as a reference mass, the mass obtained assuming no intrinsic quadrupole deformation $\langle \hat{Q}_2\rangle_{[i=1,2]} = 0$ and using the simple prescription $\langle \hat{r}^2\rangle_{[i]} = \frac{3}{5}A_i(1.2A_i^{1/3})^2$ fm$^2$. The reference mass obtained in this way is denoted by $M_{2,\rm as}$. In the following, the quadrupole mass will always be shown with respect to this mass.

In Fig. 4(a), the ratio $M_2/M_{2,\rm as}$ of quadrupole mass deduced with the present method is shown as a function of $Q_2$ along the TD-EDF trajectories for $Q_2^{\rm ini} = 160$ b. In this figure, the mass obtained using an increasing initial boost in the quadrupole collective momentum is shown. To illustrate the departure from the adiabatic path, we also show the result obtained for a given $Q_2$ assuming that the local density identifies with the corresponding density directly obtained from the constrained mean-field calculation. In the following, the latter is referred to as "static mass".

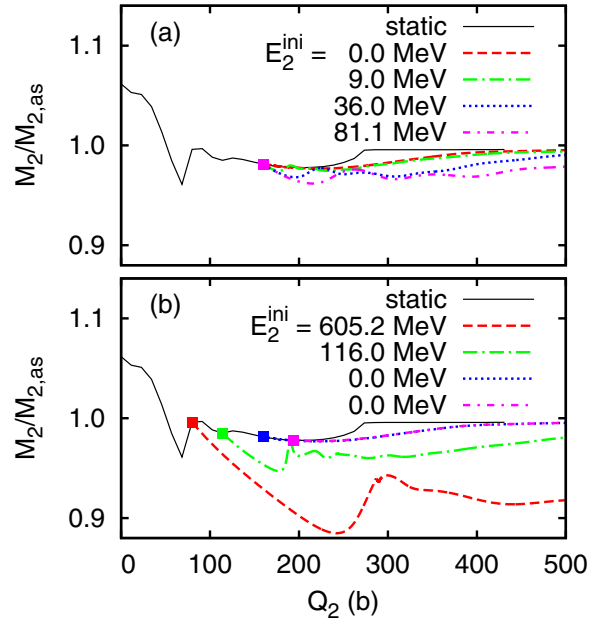


FIG. 4. (Color online) Top: Quadrupole mass parameter calculated from TD-EDF paths. In all cases, the initial quadrupole moment is $Q_2^{\rm ini} = 160$ b. Different trajectories correspond to different initial boosts. The corresponding initial collective energies $E_2^{\rm ini}$ are systematically reported in the figure. The quadrupole mass obtained using Eq. (19) assuming that the system follow the adiabatic PEC is also shown (solid line) for comparison. Bottom: Quadrupole mass obtained with varying initial quadrupole deformation, $Q_2^{\rm ini} = 80$, 114, 160, and 194 b.

We observe in Fig. 4(a) that the mass is in general rather close to the static mass, especially if $E_2^{\rm ini} = 0$ MeV. In that case, the system first follows closely the adiabatic case and then some deviation is observed. The deviation occurs around the scission point. At this point, the slope of the PEC suddenly changes to match the Coulomb case that dominates at large distance. This increase of slope is expected to induce also a larger collective velocity and therefore also induce a possible departure from the adiabatic limit. We see in this figure that the mass also depends on the initial collective velocity imposed on the system. The larger the initial velocity, the more deviation from the static mass is observed. It is however worth mentioning that the adiabatic/nonadiabatic behavior cannot easily be concluded solely from the difference of mass as will be further illustrated below.

### B. Mass parameter for $Q_2^{\rm ini} \leqslant Q_2^{\rm th}$

As we have mentioned already, TD-EDF cannot spontaneously lead to the separation of the system into two fragments

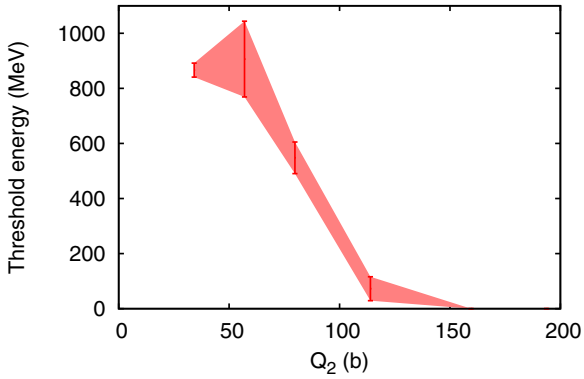


FIG. 5. (Color online) Minimum collective energy after a boost that should be initially deposited into the system to induce the fission of $^{258}$Fm for $Q_2^{\rm ini} \leqslant Q_2^{\rm th}$. This energy is plotted as a function of the initial quadrupole deformation considered. For each $Q_2$, the highest (respectively lowest) value of the initial collective energy where the scission is not (respectively is) observed is reported.

below $Q_2^{\rm th}$ due to the improper treatment of level crossing. Still it is possible to induce a fission by imposing some collective velocity initially. As already noted in Ref. [17], the collective energy that should be initially put in the system to observe fission is in general rather large. This aspect is further illustrated in Fig. 5 where we investigated systematically the minimal collective energy necessary to induce fission for selected initial quadrupole deformation. To obtain this curve, for each $Q_2^{\rm ini}$ we systematically performed TD-EDF calculation by increasing progressively the boost intensity. The error bars correspond respectively to the largest (respectively lowest) collective energy where fission is (respectively is not) observed. Note that for the two lowest $Q_2^{\rm ini}$ no binary fission is observed but ternary fission is (see also Fig. 3).

The collective energy is very high compared to the typical barrier height to fission. We would like to mention that this is clearly a pathology of TD-EDF at small initial deformation and beyond mean-field effects should clearly be included to obtain meaningful information from microscopic transport models around the fission barrier. Still, to illustrate that the present method can apply in a situation rather far from the adiabatic limit, we deduced the mass parameter for such initially highly excited systems. A few examples are shown in Fig. 4(b). In that case, important deviations are observed in the mass parameters compared to the static/adiabatic limit. Since large collective velocities are imposed initially, such deviations are not surprising. However, the difference can also stem from the fact that the initial boost can induce a motion that is not described by the simple one-dimensional energy landscape shown in Fig. 1. In particular, preparing the system using constraint mean-field + boost is a rather arbitrary choice that will induce specific motion not only in the $Q_2$ collective space but also in a larger space of collective variables like the monopole $\langle r^2 \rangle$, hexadecapole $Q_4$, etc. In particular, since the mass reported in Fig. 4 is compared for the same $Q_2$, differences observed between the static and dynamical masses stem from differences in the root-mean-square radii that ultimately come from the differences in local densities. Clear

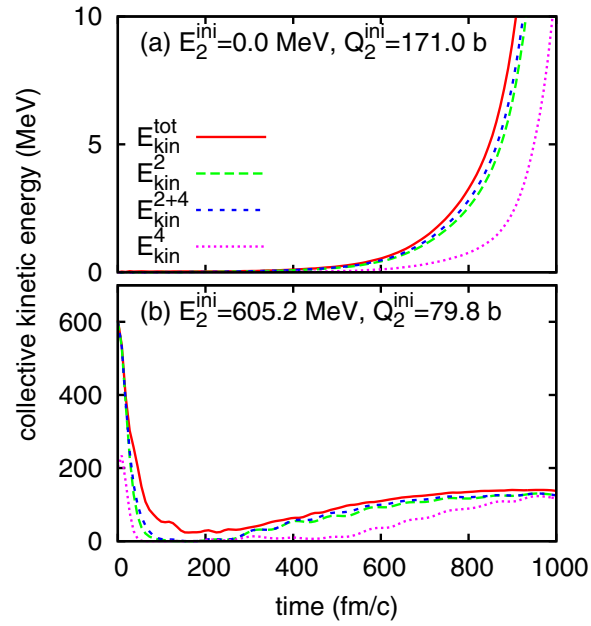


FIG. 6. (Color online) Evolution of the total collective kinetic energy $E_{\rm kin}^{\rm tot}$ as a function of time. The initial systems correspond respectively to a quadrupole moment (a) $Q_2^{\rm ini} = 171.0$ b without boost or (b) to $Q_2^{\rm ini} = 79.8$ b with initial boost. In both cases, the CKE obtained using Eq. (24) and associated to $Q_2$ only ($E_{\rm kin}^2$), $Q_4$ only ($E_{\rm kin}^4$), or both ($E_{\rm kin}^{2+4}$) are also shown.

differences are observed between densities shown in Fig. 3 and densities of the adiabatic PEC (Fig. 1). The differences in local densities can of course come from nonadiabatic effects but also from a more complex path in a multidimensional potential energy landscape that could not be simply reduced to the one-dimensional (1D) picture of Fig. 1.

### C. Total versus collective kinetic energy

As we mentioned in Sec. II, the present method allows us to access the set of conjugate momenta and the collective kinetic energy (CKE) as well as the masses associated with the set of collective coordinates. The CKE of the set of collective variables $\{Q_\alpha\}$ can be obtained following Sec. II B diagonalizing the mass matrix and using Eq. (24). Note that the diagonal and off-diagonal matrix elements of the mass are given explicitly in Appendix A.

In Fig. 6, the CKE associated to the quadrupole and/or hexadecapole moment are displayed as a function of time during the fission process. We also compare these energies to the total kinetic energy computed through

$$E_{\rm kin}^{\rm tot} = \frac{\hbar^2}{2m} \int d^3r \, \frac{\boldsymbol{j}(\boldsymbol{r},t)^2}{n(\boldsymbol{r},t)}, \tag{27}$$

where $\boldsymbol{j}(\boldsymbol{r},t)$ is the single-particle current. Two different initial conditions are considered, one starting from an already elongated shape without boost and one with a more compact shape but where a boost in quadrupole momentum is applied to induce fission.

From this figure several interesting aspects could be seen:

(i) At initial time $E^{\rm tot}_{\rm kin} = E^{2}_{\rm kin}$. This is indeed due to the fact that either the two are equal to zero [Fig. 6(a)] or that the initial condition [Fig. 6(b)] is such that all initial kinetic energy is imposed by the quadrupole boost.

(ii) The CKE associated to $Q_4$ is also initially nonzero. This stems from the fact that $Q_2$ and $Q_4$ are not independent collective variables. Therefore boosting in the quadrupole moment also induces an excitation of the hexadecapole and most probably higher order even multipole moments.

(iii) Due to the rather strong correlations between $Q_2$ and $Q_4$, the off diagonal matrix elements of the inertia play an important role. Indeed, neglecting this contribution would give

$$E^{2+4}_{\rm kin} \simeq E^{2}_{\rm kin} + E^{4}_{\rm kin}. \tag{28}$$

However, summing directly these two energies would exceed the total kinetic energy that is an upper bound whatever is the selected set of collective variables. In Fig. 6, $E^{2+4}_{\rm kin}$ accounts for the off-diagonal inertia and finally leads to an energy that is lower than $E^{\rm tot}_{\rm kin}$.

(iv) At large distances, we see that

$$E^{\rm tot}_{\rm kin} \simeq E^{2+4}_{\rm kin} \simeq E^{2}_{\rm kin}. \tag{29}$$

This is due to the fact that all kinetic energies are dominated by the relative motion of the two fragments in the exit channel.

### D. Collective evolution close to scission

Here we investigate the collective evolution close to the scission point. The scission can be seen directly on Fig. 1 by the change of slope around $Q_2^{\rm sc} \simeq 270$ b. The evolution of the collective momentum is displayed in Fig. 7 as a function of $Q_2$ for different initial deformations. We clearly see a different behavior depending on whether the initial quadrupole moment is above or below $Q_2^{\rm sc}$. As we will see below, for $Q_2^{\rm ini} \geqslant Q_2^{\rm sc}$ the momentum evolution corresponds essentially to the evolution of two escaping nuclei boosted by their mutual Coulomb field. For $Q_2^{\rm ini} \leqslant Q_2^{\rm sc}$, the nuclear interaction between nuclei still plays a significant role and a richer evolution is seen. In that case, independently of the initial $Q_2^{\rm ini}$ value, after some transition time, all curves become nearly identical with one another.

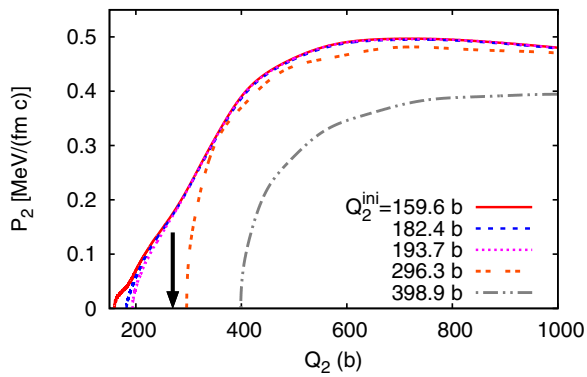


FIG. 7. (Color online) Evolution of the collective momentum as a function of time for different initial quadrupole deformations (with $Q_2^{\rm ini} \geqslant Q_2^{\rm th}$). The arrow indicates the scission point associated to the adiabatic potential.

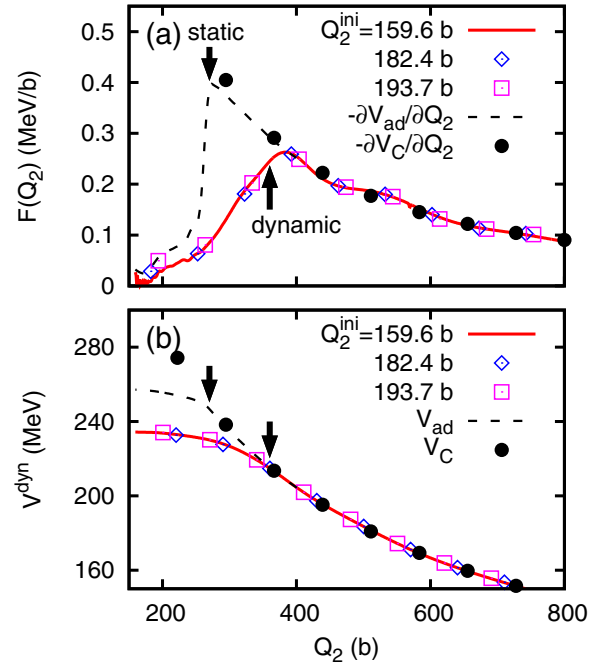


FIG. 8. (Color online) (a) Function $F(Q_2)$ obtained with TDEDF using Eq. (31) for the three evolutions with $Q_2^{\rm ini} \leqslant Q_2^{\rm sc}$ displayed in Fig. 7. For comparison, we also show the forces acting on $Q_2$ that would be induced either by the adiabatic potential (black dashed line) or solely by the Coulomb field (black filled circle). The arrows in the figure indicate the $Q_2$ value where the neck density $\rho_{\rm neck}$ becomes ten times less than the saturation density $\rho_{\rm sat} = 0.16$ fm$^{-3}$. The two arrows indicate the adiabatic path (static) and dynamical path (dynamic). In the latter case, the position where $\rho_{\rm neck}/\rho_{\rm sat} = 1/10$ is almost independent of $Q_2^{\rm ini}$. (b) Dynamical potential curve obtained by integrating $F(Q_2)$ using Eq. (35). Again for comparison, the adiabatic potential and the Coulomb field are also shown. Here, the origin of energy is taken such that $E = 0$ for $Q_2 \to \infty$.

In the absence of dissipation and assuming that the dynamics stem uniquely from a collective potential, one would expect that the smaller is $Q_2^{\rm ini}$, the higher is $P_2(t)$ as a function of $Q_2$. However, it clearly seems from Fig. 7 that part of the energy is dissipated in the early stage of the evolution. To further progress, we may follow Ref. [6] and assume that the momentum evolution can be written as a simple dissipative equation of motion:

$$\dot{P}_2 = -\frac{\partial V_{\rm coll}}{\partial Q_2} + \frac{1}{2}\frac{\partial M_2}{\partial Q_2}\dot{Q}_2^2 - \gamma(Q_2)\dot{Q}_2, \tag{30}$$

where the collective potential $V_{\rm coll}$ and the friction coefficient $\gamma$ are *a priori* unknown quantities. In the adiabatic limit, the collective potential identifies with the one shown in Fig. 1 and $\gamma(Q_2) = 0$ along the path.

To remove the possible effect of the mass evolution and eventually access the potential and dissipative collective properties, it is convenient to define the quantity

$$F(Q_2) \equiv \dot{P}_2 - \frac{1}{2}\frac{\partial M_2}{\partial Q_2}\dot{Q}_2^2. \tag{31}$$

This function is shown in Fig. 8 as a function of $Q_2$ for some of the evolutions presented in Fig. 7. If the macroscopic transport equation (30) is valid, this quantity is expected to identify with

$$F(Q_2) = -\frac{\partial V_{\rm coll}}{\partial Q_2} - \gamma(Q_2)\dot{Q}_2. \quad (32)$$

and therefore is sensitive to both the potential and dissipative part. For comparison, we also display the cases where dissipation is assumed to be zero in Eq. (32) and where the potential part identifies either to the adiabatic potential or solely to the Coulomb field. In the latter case, the Coulomb potential for large relative distance, or large $Q_2$, is approximated by

$$V_C \approx \frac{Z_1 Z_2 e^2}{R} \approx \frac{Z_1 Z_2 e^2}{\sqrt{\frac{A}{2A_1A_2}}Q_2} = \frac{1}{4}\sqrt{\frac{A}{2}}Z^2e^2Q_2^{-1/2}. \quad (33)$$

The last expression is obtained for the symmetric fission case, i.e., $Z_1 = Z_2 = Z/2$ and $A_1 = A_2 = A/2$ considered here, and further assuming no intrinsic quadrupole deformation of emitted fragments after scission.

Figure 8(a) gives interesting information on the different steps leading to fission. We first see that after the very first instant of the evolution where some dissipation occurred, all evolutions obtained with $Q_2^{\rm ini} \leqslant Q_2^{\rm sc}$ are on top of each other. The dynamic before scission deviates significantly from the expected adiabatic one underlining the importance of both nonadiabatic and dissipative effects. In particular, we clearly see that the dynamical formation of the neck differs from the adiabatic case. Defining the scission point as the $Q_2$ value where the neck density equals $1/10$ of the saturation density, we observe that dynamically the scission occurs at much larger $Q_2$ than the adiabatic case (arrows in Fig. 8). This has two consequences: (i) First, the two nuclei stick together at a larger distance compared to the adiabatic case. Accordingly, the nuclear field can play an enhanced role. (ii) We see that we should introduce the notion of "dynamical scission point" that *a priori* differs from the "adiabatic scission point" and that occurs at a larger quadrupole moment. In the present case of symmetric compact fission, the dynamical scission point occurs around $Q_2^{\rm sc,dyn} \simeq 360$ b, compared to the adiabatic scission point $Q_2^{\rm sc,stat} \simeq 270$ b.

After scission, the dynamical evolution is very close to the Coulomb field case (black filled circles). This indicates that no dissipation takes place after this point and that the dissipation mainly occurs at the initial time of the calculation. For large $Q_2$, we clearly observe some oscillations around the average Coulomb repulsion that could be attributed to the dynamical oscillation of the intrinsic shapes of each nucleus. These oscillations obviously go beyond the simple macroscopic approximation (30) since they involve additional intrinsic shape degrees of freedom.

Following [6], one could *a priori* use $F(Q_2)$ to get the potential energy landscape as well as the friction coefficient along the path. However, the method used in Ref. [6] that consists in performing two evolutions with close initial conditions cannot be applied here due to the fact that the collective velocity becomes rapidly independent of $Q_2^{\rm ini}$. Figure 7 seems however to indicate that dissipation occurs only at rather small $Q_2$. For $Q_2 > 300$ b, one might assume that the motion is only driven by a potential denoted by $V^{\rm dyn}(Q_2)$. Then, we have the approximate relationship

$$\frac{\partial V^{\rm dyn}(Q_2)}{\partial Q_2} = -F(Q_2), \quad (34)$$

where $F(Q_2)$ is estimated along the path using Eq. (31). To get the potential itself, one should fix the boundary condition. We know from Fig. 8(a) that the potential identifies to a good approximation with the Coulomb potential after the scission. The potential can eventually be obtained through the relation

$$V^{\rm dyn}(Q_2) = V_C\left(Q_2^{\rm max}\right) + \int_{Q_2}^{Q_2^{\rm max}} F(Q_2')dQ_2', \quad (35)$$

where $Q_2^{\rm max}$ is taken much larger than the dynamical scission point. Note that we do not take into account here the excitation energy of the fragments. Some examples of the potential obtained in this way are shown in Fig. 8(b) assuming $Q_2^{\rm max} = 800$ b. $V_{\rm ad}$ shown by the dashed curve in Fig. 8(b) is drawn by shifting the PEC given in Fig. 1 so that it coincides with $V_C$ at $Q_2 = 433$ b ($\geqslant Q_2^{\rm sc,stat}$) and thus $V_{\rm ad} \to 0$ for $Q_2 \to \infty$.

We see in Fig. 8(b) that the potential obtained using Eq. (35) differs significantly from the adiabatic one at small $Q_2$ due to dynamics and eventually nonadiabatic effects. Note that the dynamical potential should be interpreted with some caution since it might contain some dissipative effects especially at initial time. It is worth in particular mentioning that the adiabatic and dynamical potentials should be identical at initial $Q_2$. We clearly observe in Fig. 8(b) a lower value for the dynamical case. The difference between the adiabatic and dynamical curves at $t = 0$ corresponds to the energy transferred into the other collective degrees freedom or internal excitations during the fission. We see that this difference is $\approx$23 MeV for $Q_2^{\rm ini} = 160$ b.

### E. Dissipation estimated from energy balance

Alternatively, in order to estimate the energy dissipated into the internal excitation of the fragments, an analysis similar to Ref. [16] has been made for the total kinetic energy (TKE) of the outgoing fragments after fission. The TKE is defined as

$$\text{TKE} = \frac{1}{2}\mu\dot{R}^2 + \frac{Z_1Z_2e^2}{R} \equiv T_{\rm rel} + V_C(R) \quad (36)$$

at large $R$ well beyond the scission point. Note that the TKE is the energy of the relative motion between the fragments at infinite separation, and it is not the same quantity as either Eq. (24) or Eq. (27), which may contain the internal excitation energy of the fragments. The energy dissipated into the DOFs other than the relative motion, or the excitation energy of fragments, is then given by $E^* = E_0 - \text{TKE}$, where $E_0$ is the total energy of the system [16]. Note that the origin of energy for $E_0$ is taken as that for $R(t) \to \infty$ with fragments staying at their ground states.

In Fig. 9 we show relative kinetic energy $T_{\rm rel}$, the Coulomb energy $V_C$, and the total kinetic energy (TKE) of the fission fragments as a function of the relative distance $R$ for the

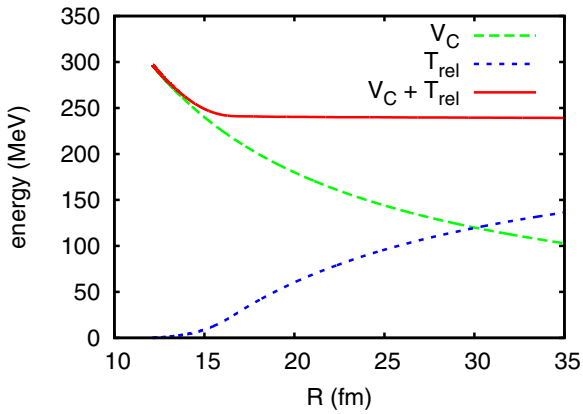


FIG. 9. (Color online) The relative kinetic energy $T_{\rm rel}$, the Coulomb energy $V_C$, and the total kinetic energy (TKE) of the fission fragments as a function of the relative distance $R$ for $Q_2^{\rm ini} = 197$ b.

evolution with $Q_2^{\rm ini} = 194$ b. We see a plateau in TKE for large $R$ at ≈238 MeV, which is identified as the TKE for this process, while the total energy of the system is $E_0 \approx 256$ MeV, which is given by the value of $V_{\rm ad}$ in Fig. 8(b) at $Q_2^{\rm ini}$. Taking the difference, we obtain $E^* \approx 18$ MeV. This is close to the value obtained from the previous analysis confirming that the difference between the adiabatic potential and the dynamical potential estimated from Eq. (35) most likely stems from the energy dissipated along the fission path.

## IV. CONCLUSION

In the present work, a method is proposed to construct conjugated collective momenta associated to a given set of local collective variables along a time-dependent EDF path. A detailed discussion is made on the proper definition of associated inertia including the effect of its possible off-diagonal matrix elements. Once pairs of conjugated collective variables are obtained, one can make a macroscopic reduction of the microscopic mean-field dynamic.

An illustration is given here with the fission process. A precise analysis is made in the symmetric fission of $^{258}$Fm. The mass matrix is calculated along the fission path including only the quadrupole moment, and/or both the quadrupole and hexadecapole moments. In particular, the important role of off-diagonal matrix elements of the mass is underlined. Then, a detailed analysis of the macroscopic evolution in the quadrupole collective space is made. The importance of dissipation in the early stage of the evolution is discussed. Clear nonadiabatic effects are probed, in particular associated with the specific neck evolution. We show that the scission point, called dynamical scission point, occurs at a much larger quadrupole moment compared to that for the adiabatic path. An attempt to extract the nucleus-nucleus potential felt by the daughter nuclei after fission is also made. It is shown that this potential significantly differs from the adiabatic one due to the nonadiabatic effects and the dissipation of energy into the intrinsic excitations of fission fragments.

The method presented here is rather versatile and could be used in other dynamical processes. For instance, it could *a priori* be used to study anharmonicity in giant resonances as well as possible coupling between collective modes.

TABLE I. Multipole operators $\hat{Q}_\lambda = \sqrt{\frac{16\pi}{2\lambda+1}}\hat{r}^\lambda \hat{Y}_{\lambda 0}$ for $\lambda = 2,3,4,5,6$.

| λ | Operator |
|---|---|
| 2 | $2\hat{z}^2 - \hat{x}^2 - \hat{y}^2$ |
| 3 | $2\hat{z}^3 - 3\hat{z}\hat{x}^2 - 3\hat{y}^2\hat{z}$ |
| 4 | $\frac{1}{4}(35\hat{z}^4 - 30\hat{r}^2\hat{z}^2 + 3\hat{r}^4)$ |
| 5 | $\frac{1}{4}(63\hat{z}^5 - 70\hat{r}^2\hat{z}^3 + 15\hat{r}^4\hat{z})$ |
| 6 | $\frac{1}{8}(231\hat{z}^6 - 315\hat{r}^2\hat{z}^4 + 105\hat{r}^4\hat{z}^2 - 5\hat{r}^6)$ |

### ACKNOWLEDGMENTS

We would like to thank G. Adamian, N. Antonenko, S. Ayik, and K. Hagino for useful discussions on collective observables. G.S. acknowledges the Japan Society for the Promotion of Science for the JSPS postdoctoral fellowship for foreign researchers. This work was supported by Grant-in-Aid for JSPS Fellows No. 14F04769.

## APPENDIX A: GENERAL FORMULA FOR THE INERTIA MATRIX

In this Appendix we give the explicit expression for the inertia matrix

$$\frac{m}{M_{\alpha\beta}} = \mathrm{Tr}[\rho \nabla Q_\alpha \cdot \nabla Q_\beta], \tag{A1}$$

associated with the general multipole moment

$$\hat{Q}_\lambda = \sqrt{\frac{16\pi}{2\lambda+1}}\hat{r}^\lambda \hat{Y}_{\lambda 0}. \tag{A2}$$

Its expressions for $2 \leqslant \lambda \leqslant 6$ are given in Table I.

Using the Racah algebra technique, one obtains the following for the matrix:

$$\frac{m}{M_{\lambda\lambda'}} = \sum_L (2L+1)\frac{(s-2L)!(s-2\lambda)!(s-2\lambda')!(s/2)!(s/2-1)!}{(s-1)!(s/2-L)!(s/2-L-1)![(s/2-\lambda)!]^2[(s/2-\lambda')!]^2}\langle \hat{r}^{\lambda+\lambda'-2-L}\hat{Q}_L\rangle, \tag{A3}$$

where $s = \lambda + \lambda' + L$ and the value of $L$ runs over $L = |\lambda - \lambda'|, |\lambda - \lambda'| + 2, |\lambda - \lambda'| + 4, \ldots, \lambda + \lambda' - 2$. It allows us to compute a matrix element for any multipolarities λ and λ′. In Table II we illustrate expressions of the matrix elements for

TABLE II. Illustration of the inertia matrix elements $m/M_{\lambda\lambda'}$ for the multipoles of $\lambda,\lambda' = 2,3,4$. The expressions for the multipole operators are given in Table I.

| $\lambda\backslash\lambda'$ | 2 | 3 | 4 |
|---|---|---|---|
| 2 | $4(2\langle\hat{r}^2\rangle + \langle\hat{Q}_2\rangle)$ | $\frac{12}{5}(3\langle\hat{r}^2\hat{Q}_1\rangle + 2\langle\hat{Q}_3\rangle)$ | $\frac{8}{7}(9\langle\hat{r}^2\hat{Q}_2\rangle + 5\langle\hat{Q}_4\rangle)$ |
| 3 | | $\frac{12}{7}(7\langle\hat{r}^4\rangle + 4\langle\hat{r}^2\hat{Q}_2\rangle + 3\langle\hat{Q}_4\rangle)$ | $\frac{8}{77}(99\langle\hat{r}^4\hat{Q}_1\rangle + 77\langle\hat{r}^2\hat{Q}_3\rangle + 150\langle\hat{Q}_5\rangle)$ |
| 4 | | | $\frac{8}{231}(462\langle\hat{r}^6\rangle + 275\langle\hat{r}^4\hat{Q}_2\rangle + 243\langle\hat{r}^2\hat{Q}_4\rangle + 175\langle\hat{Q}_6\rangle)$ |

some important multipoles 2, 3, and 4, which are related to elongation, mass asymmetry, and size of neck, respectively.

## APPENDIX B: DEFINITION OF NEW OPERATORS $(\hat{Q}'_\alpha, \hat{P}'_\alpha)$

In this Appendix, we give some intermediate steps to obtain operators that fulfill the commutation rules (23) along the TD-EDF trajectory.

The real-space representation of the momentum operator conjugated to the coordinate $\hat{Q}_\alpha$ is given by

$$P_\alpha = -i\hbar\frac{M_{\alpha\alpha}}{m}\left(\frac{\nabla^2 Q_\alpha}{2} + \nabla Q_\alpha\cdot\nabla\right). \tag{B1}$$

Accordingly, we have

$$\langle[\hat{Q}_\alpha,\hat{P}_\beta]\rangle = i\hbar\frac{M_{\beta\beta}}{m}\mathrm{Tr}[\rho(t)\nabla Q_\alpha\cdot\nabla Q_\beta].$$

Introducing the mass matrix elements $m/M_{\alpha\beta} \equiv \mathrm{Tr}[\rho(t)\nabla Q_\alpha\cdot\nabla Q_\beta]$, the above expression can be written as

$$\langle[\hat{Q}_\alpha,\hat{P}_\beta/M_{\beta\beta}]\rangle = i\hbar\frac{1}{M_{\alpha\beta}}. \tag{B2}$$

We introduce the orthogonal matrix $W$ that diagonalizes the mass, i.e.,

$$\sum_{\alpha\beta} W_{k\alpha}\frac{1}{M_{\alpha\beta}}W^T_{\beta l} = \delta_{kl}\frac{1}{M'_k}, \tag{B3}$$

where $1/M'_k$ is the eigenvalue of the inertia tensor. Then we have

$$\sum_{\alpha\beta} W_{k\alpha}W^T_{\beta l}\langle[\hat{Q}_\alpha,\hat{P}_\beta/M_{\beta\beta}]\rangle = i\hbar\delta_{kl}\frac{1}{M_k}. \tag{B4}$$

Introducing the new set of conjugated operators

$$\hat{Q}'_k = \sum_\alpha W_{k\alpha}\hat{Q}_\alpha, \quad \text{and} \quad \hat{P}'_k = M'_k\sum_\alpha W_{k\alpha}\frac{\hat{P}_\alpha}{M_{\alpha\alpha}}, \tag{B5}$$

we see that these operators respect the desired commutation relation

$$\langle[\hat{Q}'_k,\hat{P}'_l/M'_l]\rangle = i\hbar\delta_{kl}\frac{1}{M'_k} \tag{B6}$$

or equivalently

$$\langle[\hat{Q}'_k,\hat{P}'_l]\rangle = i\hbar\delta_{kl}. \tag{B7}$$


[1] K.-H. Kim, T. Otsuka, and P. Bonche, J. Phys. G **23**, 1267 (1997).
[2] C. Simenel, Ph. Chomaz, and G. de France, Phys. Rev. Lett. **86**, 2971 (2001).
[3] T. Nakatsukasa and K. Yabana, Phys. Rev. C **71**, 024301 (2005).
[4] J. A. Maruhn, P.-G. Reinhard, P. D. Stevenson, J. R. Stone, and M. R. Strayer, Phys. Rev. C **71**, 064328 (2005).
[5] A. S. Umar and V. E. Oberacker, Phys. Rev. C **71**, 034314 (2005).
[6] K. Washiyama and D. Lacroix, Phys. Rev. C **78**, 024610 (2008).
[7] R. Vandenbosch and J. R. Huizenga, *Nuclear Fission* (Academic, New York, 1973).
[8] J. W. Negele, Nucl. Phys. A **502**, 371c (1989).
[9] H. Goutte, J. F. Berger, P. Casoli, and D. Gogny, Phys. Rev. C **71**, 024316 (2005).
[10] B. Avez, C. Simenel, and Ph. Chomaz, Phys. Rev. C **78**, 044318 (2008).
[11] S. Ebata, T. Nakatsukasa, T. Inakura, K. Yoshida, Y. Hashimoto, and K. Yabana, Phys. Rev. C **82**, 034306 (2010).
[12] I. Stetcu, A. Bulgac, P. Magierski, and K. J. Roche, Phys. Rev. C **84**, 051309 (2011).
[13] G. Scamps, D. Lacroix, G. F. Bertsch, and K. Washiyama, Phys. Rev. C **85**, 034328 (2012).
[14] Y. Hashimoto, Eur. Phys. J. A **48**, 1 (2012).
[15] G. Scamps and D. Lacroix, Phys. Rev. C **87**, 014605 (2013).
[16] C. Simenel and A. S. Umar, Phys. Rev. C **89**, 031601 (2014).
[17] Ph. M. Goddard, Ph.D. thesis, University of Surrey, 2014.
[18] P. M. Goddard, P. D. Stevenson, and A. Rios, arXiv:1504.00919.
[19] G. Scamps, C. Simenel, and D. Lacroix, Phys. Rev. C **92**, 011602(R) (2015).
[20] C. Simenel, D. Lacroix, and B. Avez, *Quantum Many-Body Dynamics: Applications to Nuclear Reactions* (VDM Verlag, Sarrebruck, Germany, 2010).
[21] G. F. Bertsch and H. Feldmeier, Phys. Rev. C **56**, 839 (1997).
[22] P.-G. Reinhard, K. Goeke, and R. Y. Cusson, Z. Phys. A **295**, 45 (1980).
[23] P.-G. Reinhard, M. Brack, and O. Genzken, Phys. Rev. A **41**, 5568 (1990).
[24] P.-G. Reinhard and Y.-K. Gambhir, Ann. Phys. **504**, 598 (1992).
[25] G. G. Adamian, N. V. Antonenko, and R. V. Jolos, Nucl. Phys. A **584**, 205 (1995).
[26] P. Bonche, H. Flocard, and P. H. Heenen, Comput. Phys. Commun. **171**, 49 (2005).
[27] G. Scamps and D. Lacroix, Phys. Rev. C **88**, 044310 (2013).
[28] G. Scamps and D. Lacroix, Phys. Rev. C **89**, 034314 (2014).